

Research Paper

A Hybrid Finite Element Method – Kirchhoff Approximation Method for Modeling Acoustic Scattering from an Underwater Vehicle Model with Alberich Coatings with Periodic Internal Cavities

Fan YANG⁽¹⁾, Zilong PENG^{(1),(3)*}, Hao SONG⁽²⁾, Yuhang TANG⁽³⁾, Xuhong MIAO⁽³⁾

⁽¹⁾ School of Energy and Power, Jiangsu University of Science and Technology
Zhenjiang, China

⁽²⁾ Systems Engineering Research Institute
Beijing, China

⁽³⁾ PLA Unit 92578
Beijing, China

*Corresponding Author e-mail: zlp_just@sina.com

(received July 17, 2023; accepted November 25, 2023; published online February 20, 2024)

Anechoic tiles can significantly reduce the echo intensity of underwater vehicles, thereby increasing the difficulty of detecting such vehicles. However, the computational efficiency of conventional methods such as the finite element method (FEM) and the boundary element method (BEM) has its limitations. A fast hybrid method for modeling acoustic scattering from underwater vehicles with anechoic tiles with periodic internal cavities, is developed by combining the Kirchhoff approximation (KA) and FEM. The accuracy and rapidity of the KA method were validated by FEM. According to the actual situation, the reflection coefficients of rubber materials with two different structures under rigid backing are simulated by FEM. Using the KA method, the acoustic scattering characteristics of the underwater vehicle with anechoic tiles are obtained by inputting the reflection coefficients and the target's geometric grid. Experiments on the monostatic target strength (TS) in the frequency range of 1 to 20 kHz and time domain echo characteristics of acoustic scattering on a benchmark scale model with anechoic tiles are conducted. The research results indicate that the TS values and echo characteristic curves of the KA solutions closely approximate the experimental results, which verifies the accuracy of the KA method in calculating the TS and echo characteristics of underwater vehicles with anechoic tiles.

Keywords: anechoic tile; Kirchhoff approximation; target strength; echo characteristic.



Copyright © 2024 The Author(s).
This work is licensed under the Creative Commons Attribution 4.0 International CC BY 4.0
(<https://creativecommons.org/licenses/by/4.0/>).

1. Introduction

Anechoic tiles are widely used in underwater combat platforms such as underwater vehicles. In the underwater acoustic environment, considering the influence of temperature, salinity, pressure, and viscosity (WITOS, 2019; ESFAHANI *et al.*, 2023; ESFAHANI, SUN, 2023), laying the anechoic tiles on the submarine's surface not only absorbs incident sound waves but also reduces structural noise. Therefore, anechoic tiles play an important role in the acoustic stealth of

underwater vehicles (YAO *et al.*, 2007; HUANG *et al.*, 2015; XU *et al.*, 2004). With the development of modern sonar technology and in-depth research of acoustic stealth technology around the world, studying acoustic scattering and echo characteristics simulation of underwater vehicles equipped with anechoic tiles has become a crucial mission.

Many scholars have studied the scattered sound field of underwater complex targets using numerical methods such as finite element method (FEM) and boundary element method (BEM). In 2013, WEI *et al.*

simulated the acoustic scattering of rigid spheres and infinite cylinders based on BEM. In 2015, XU *et al.* used the BASIS method to simulate the scattering of the BeTSSi model at a frequency of 200 Hz. In 2018, FENG *et al.* employed BEM to analyze the target strength (TS) of the rigid boundary benchmark model in the low-frequency range. In the same year, CHEN and LUO (2018) deduced the Helmholtz formula for the scattered sound field of underwater targets based on the boundary element theory.

FEM and BEM require extremely dense meshes to ensure accurate calculation, and this mesh density increases with higher computing frequencies (LIU *et al.*, 2019). As the mesh density increases, the computational time for both methods at high frequencies progressively extends. To solve this problem, FAN and TANG (1999) proposed a Kirchhoff approximation (KA) method for calculating TS. Subsequently, FAN and ZHUO (2006) introduced a KA method for graphic visualization, considering occlusion, secondary scattering (ZHENG *et al.*, 2011; MARSTON, SUN, 1995), ray tracing, and multiple iterations (WANG *et al.*, 2021).

LEE and SEONG (2009) derived the time domain solution of Kirchhoff's formula for impedance polygons. PIGNIER *et al.* (2015) used the KA formula to study multiple scattering problems of external radiation noise from moving ground vehicles through objects such as roads, buildings, and noise-shields. ABAWI (2016) used KA to establish a method for solving the frequency and time domain solutions of scattered sound fields from arbitrarily shaped targets. To improve the computational speed of the KA method, LAVIA *et al.* (2018) proposed the concept of replacing the flat facets with curved triangles. Additionally, LIU *et al.* (2023) established a highlight model that can reflect the real lines and scattering characteristics of underwater vehicles.

The traditional KA method is primarily applied to calculate the echo intensity of rigid targets. While FEM can solve the acoustic scattering problem of the targets laying anechoic tiles, the modeling process becomes increasingly time-consuming, especially when dealing with complex anechoic tiles and the varying shapes of underwater vehicles. Therefore, whether it is modeling or calculation, FEM will require a substantial time investment. In this paper, the reflection coefficients of anechoic tiles with periodic cavities are calculated by FEM at different angles and frequencies. To overcome the time constraints associated with FEM, we integrate the target grid information and reflection coefficient matrix into the KA method, originally designed for rigid targets. This enables the quick and accurate calculation of the TS for models with anechoic tiles containing periodic internal cavities. By combining FEM and the KA method, the modeling work of laying anechoic tile on the submarine model

can be omitted, and the spatial characteristics of the scattered sound field are studied.

2. Theoretical research and calculation model

2.1. Physical method of geometrical acoustic scattering of underwater target

As shown in Fig. 1, the plane wave is incident from M_1 to the surface s , then the scattered acoustic potential function satisfies the following Helmholtz integral equation (FAN *et al.*, 2012):

$$\phi_s = \frac{1}{4\pi} \int_s \left[\phi_s \frac{\partial}{\partial \mathbf{n}} \left(\frac{e^{ikr_2}}{r_2} \right) - \frac{\partial \phi_s}{\partial \mathbf{n}} \frac{e^{ikr_2}}{r_2} \right] ds, \quad (1)$$

where s is the surface of the scatterer, \mathbf{n} is the external normal of the surface, $k = 2\pi f/c$, where the sound velocity c is a nonlinear function of temperature, ambient pressure, and salinity. In the case of free sound field and horizontal detection, where the target, transducer, and hydrophone are all situated at the same depth, the sound velocity under the circumstances can be considered constant; \mathbf{r}_1 and \mathbf{r}_2 are the incident point radius vector and the scattering point radius vector, respectively; θ_1 is the angle between \mathbf{r}_1 and \mathbf{n} , θ_2 is the angle between \mathbf{r}_2 and \mathbf{n} .

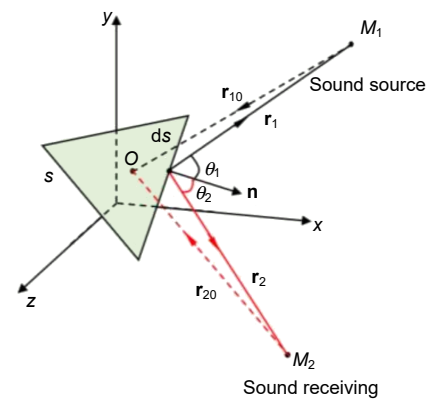


Fig. 1. Schematic diagram of the integral region, where O is the origin of coordinates, generally considered to be the geometric center of the target. The light green triangle ds represents the integral grid. Point M_1 represents the sound source, and point M_2 represents the sound receiving point.

In the monostatic configuration, where $\mathbf{r}_1 = \mathbf{r}_2 = \mathbf{r}$, $\theta_2 = \theta_1 = \theta$, and A is the amplitude, the far-field scattered sound field ϕ_s can be approximated as (FAN *et al.*, 2012):

$$\phi_s = -\frac{A}{2\pi} \int_s e^{ik2r} \left(\frac{ik\mathbf{r} - 1}{r^3} \cos\theta \right) ds. \quad (2)$$

For near-field acoustic scattering, considering the plate shown in Fig. 2, point o is the target's center and origin of coordinates. Point c , selected as a reference point on the plate, has a vector diameter denoted

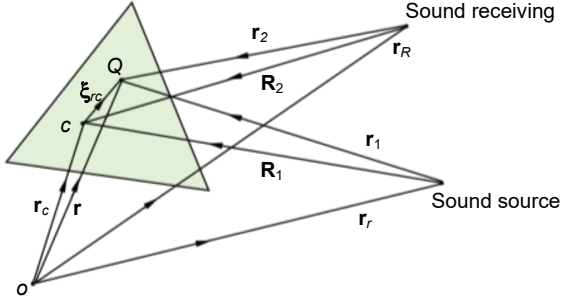


Fig. 2. Near-field sound scattering.

as \mathbf{r}_c , commonly representing the geometric center of the plate. Point Q is an arbitrary point on the plate. The vector diameter from point o to point Q is \mathbf{r} , the vector diameter of the transmitting transducer is \mathbf{r}_T , and the vector diameter of the receiving transducer is \mathbf{r}_R . There are $\mathbf{r}_1 = \mathbf{r} - \mathbf{r}_T$, unit vector $\mathbf{r}_{10} = (\mathbf{r} - \mathbf{r}_T)/r_1$; $\mathbf{r}_2 = \mathbf{r} - \mathbf{r}_R$, unit vector $\mathbf{r}_{20} = (\mathbf{r} - \mathbf{r}_R)/r_2$; $\mathbf{R}_1 = \mathbf{r}_c - \mathbf{r}_T$, unit vector $\mathbf{R}_{10} = (\mathbf{r}_c - \mathbf{r}_T)/R_1$; $\mathbf{R}_2 = \mathbf{r}_c - \mathbf{r}_R$, unit vector $\mathbf{R}_{20} = (\mathbf{r}_c - \mathbf{r}_R)/R_2$.

Where \mathbf{n} is the unit normal vector of the plate. For small plates, it can be considered that the incident sound wave is a plane wave, allowing for the following approximations: $\mathbf{r}_1 \approx \mathbf{R}_1 = |\mathbf{r}_c - \mathbf{r}_T|$, $\mathbf{r}_{10} \approx \mathbf{R}_{10}$, $\mathbf{r}_2 \approx \mathbf{R}_2 = |\mathbf{r}_c - \mathbf{r}_R|$, $\mathbf{r}_{20} \approx \mathbf{R}_{20}$; $\mathbf{r}_1 \approx \mathbf{R}_1 - \mathbf{R}_{10} \cdot \boldsymbol{\xi}_{rc}$, $\mathbf{r}_2 \approx \mathbf{R}_2 - \mathbf{R}_{20} \cdot \boldsymbol{\xi}_{rc}$, $\boldsymbol{\xi}_{rc} = \mathbf{r} - \mathbf{r}_c$.

In the monostatic configuration, the near-field scattered sound field ϕ_{sm} is

$$\phi_{sm} = -\frac{A}{2\pi} e^{i2k\mathbf{R}_1} \frac{ik\mathbf{R}_1 - 1}{\mathbf{R}_1^3} \mathbf{n} \cdot \mathbf{R}_{10} \int_s e^{-2ik\mathbf{R}_{10} \cdot \boldsymbol{\xi}_{rc}} ds. \quad (3)$$

For the near-field KA method, the key to the aforementioned formula is to find the area integral:

$$I = \int_s e^{-2ik\mathbf{R}_{10} \cdot \boldsymbol{\xi}_{rc}} ds. \quad (4)$$

Assuming that the integral plane is a plane polygon s_0 in the XOY plane, and the normal of the plane is $\mathbf{R}_{10} = u'\mathbf{i} + v'\mathbf{j} + w'\mathbf{k}$, $\boldsymbol{\xi}_{rc} = x\mathbf{i} + y\mathbf{j}$, then the integral operation above can be converted to a summation for an exact expression of the result by the following equation (LIU, 2020):

$$\begin{aligned} I_p &= \int_{s_0} e^{2ik(u'x + v'y)} dx dy \\ &= \sum_{n=1}^3 \frac{e^{-i(x_n u' + y_n v')}}{(u' + P_{n-1}v')(u' + P_n v')}, \end{aligned} \quad (5)$$

and $u' = 2ku$, $v' = 2kv$, $w' = w$, $p_1 = \frac{y_2 - y_1}{x_2 - x_1}$, $p_2 = \frac{y_3 - y_2}{x_3 - x_2}$, $p_3 = \frac{y_1 - y_3}{x_1 - x_3}$, $p_0 = \frac{y_1 - y_3}{x_1 - x_3}$, where n is the number of polygon vertices and (x_n, y_n) is the coordinates of polygon vertices.

The coordinates of points in the original coordinate system are transformed into a new coordinate system. A coordinate transformation is performed for points 1, 2, 3 to obtain their coordinates in the new coordinate system, which are $x_2(n)$, $y_2(n)$, $z_2(n)$ ($n = 1, 2, 3$). In the new coordinate system, the unit vector from the receiving point to the center of the plate is represented as $u'\mathbf{i} + v'\mathbf{j} + w'\mathbf{k}$, with $u' = 2ku$, $v' = 2kv$, $w' = w$, $k = 2\pi f/1500$.

According to the transformation of $x_2(n)$, $y_2(n)$, $z_2(n)$ ($n = 1, 2, 3$),

$$\phi = w \sum_{n=1}^3 e^{-i(x_2(n) + y_2(n))} \frac{p_{n-1} - p_n}{(u' + p_{n-1}v')(u' + p_n v')}, \quad (6)$$

and $p_1 = \frac{y_2(2) - y_2(1)}{x_2(2) - x_2(1)}$, $p_2 = \frac{y_2(2) - y_2(2)}{x_2(3) - x_2(2)}$, $p_3 = \frac{y_2(1) - y_2(3)}{x_2(1) - x_2(3)}$, $p_0 = p_3$.

2.2. Research on time domain echo characteristics of target based on the linear transfer network model

In the framework of linear acoustics, the problem of target scattering can be described using acoustic transfer theory. The target can be regarded as a linear time-invariant network. In this network, the incident signal is the input, and the echo signal is the output. The time-domain transfer function of this linear transfer network is $h(\tau, \mathbf{r}_1, \mathbf{r}_2, \boldsymbol{\rho})$, where τ is the delay, \mathbf{r}_1 and \mathbf{r}_2 are the radius vector of the incident and scattering point, respectively, and $\boldsymbol{\rho}$ is the radius vector of the target. The frequency domain transfer function $H(f, \mathbf{r}_1, \mathbf{r}_2, \boldsymbol{\rho})$ of the transfer network is denoted as the ratio of the scattering wave potential function to the incident wave potential function, where f is the frequency. In the monostatic configuration, $\mathbf{r}_1 = \mathbf{r}_2$, and the transfer functions in the time domain and frequency domain are $h(\tau, \mathbf{r}, \boldsymbol{\rho})$ and $H(f, \mathbf{r}, \boldsymbol{\rho})$, respectively.

When $x(t)$ represents the time-domain incident signal, $X(f)$ represents the frequency-domain incident signal, and $Y(f)$ represents the frequency domain echo signal. The time domain echo signal of the target can be expressed as (LIU, 2020):

$$y(t) = x(t) \otimes h(\tau, \mathbf{r}, \boldsymbol{\rho}), \quad (7)$$

where \otimes denotes the convolution operation. Then, the echo signal in the frequency domain is given by:

$$Y(f) = X(f) \cdot H(f, \mathbf{r}, \boldsymbol{\rho}), \quad (8)$$

$$y(t) = F^{-1}[Y(f)]. \quad (9)$$

The time-domain echo signal can be obtained by taking the inverse Fourier transform of the frequency-domain signal. This framework allows for the indirect extraction of the time-domain echo characteristics of underwater targets by calculating the frequency-domain signals.

2.3. Materials and model

Achieving semi-infinite air and water by adding a perfectly matched layer, the materials used are shown in Table 1.

In Fig. 3, the benchmark model (NELL, GILROY, 2003) is chosen for conducting the acoustic scattering and TS prediction of the target after laying different anechoic tiles.

The acoustic wave is incident horizontally, and the specific parameters of the benchmark model are shown

in Fig. 3b. To satisfy the far field condition, the simulated distance is 10 km.

2.4. Application of Floquet theory in solving acoustic scattering from elastomers

The challenge of the FEM in solving the acoustic scattering problem lies in the inability to create infinitely long waveguides. As shown in Fig. 4a, Floquet-Bloch theory imposes boundary conditions on the com-

Table 1. Material parameters.

Material	Density [kg/m ³]	Young's modulus [Pa]	Poisson ratio	Sound velocity [m/s]	Thickness [mm]
Rubber (Xu <i>et al.</i> , 2004)	1090	$3 \times 10^7 (1 + 0.249i)$	0.49	–	50
Steel	7800	2.13×10^{11}	0.3	–	8
Water	1000	–	–	1500	Semi-infinite
Air	1.21	–	–	343	Semi-infinite

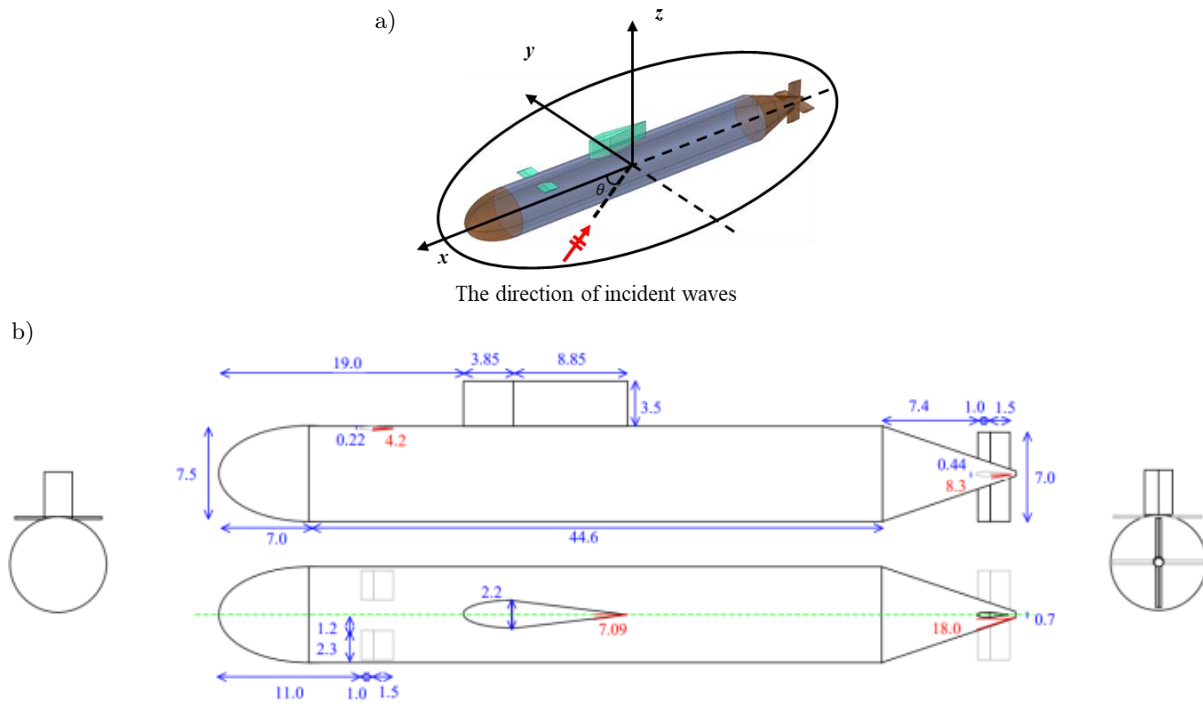


Fig. 3. a) Benchmark model and incident direction of the plane wave; b) specific dimensions of the benchmark submarine.

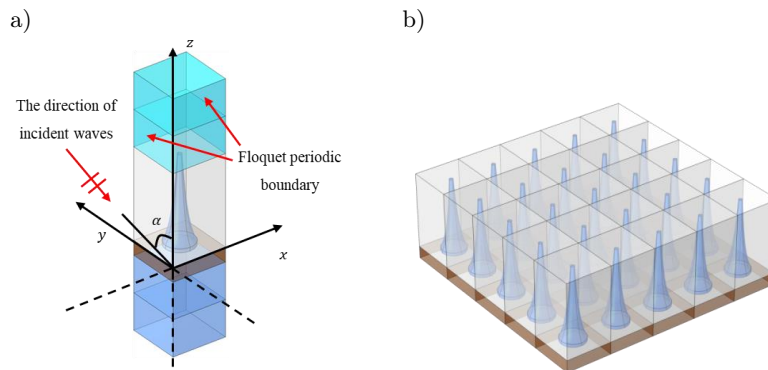


Fig. 4. a) Computational unit; b) schematic diagram of multiple units.

putational unit to simulate infinitely long waveguides. In the FEM, the equation is (TONG *et al.*, 2020):

$$\mathbf{u}_{\text{dst}}(x, y) = \mathbf{u}_{\text{src}}(x, y)e^{-i\mathbf{k}_F(\mathbf{r}_{\text{dst}}-\mathbf{r}_{\text{src}})}, \quad (10)$$

where \mathbf{u}_{src} and \mathbf{r}_{src} are the displacement and coordinate of the source boundary, and \mathbf{u}_{dst} and \mathbf{r}_{dst} are the displacement and coordinate of the target boundary. Floquet periodic boundary conditions are applied on both sides of the model, and different traveling wave numbers \mathbf{k}_F are input to simulate the finite length region as an infinite length waveguide. The anechoic tile model after incorporating the Floquet periodic condition along with a schematic diagram of multiple units are shown in Fig. 4.

2.5. Validation of the KA method

To determine the accuracy and efficiency of the KA method in calculating the acoustic scattering from the target equipped with anechoic tiles with air cavities, a verification study was conducted. In Fig. 5a, a cylindrical shell with a radius of 0.2 m, height of 1 m, and thickness of 0.008 m is selected. The cylindrical shell is made of steel with air inside, there are several anechoic tiles, each 0.05 m thick with a grating spacing of 0.03 m outside the cylindrical shell. The center of each anechoic tile contains a longitudinally cylindrical cav-

ity with a radius of 0.005 m and a height of 0.025 m. The domain being studied is meshed with tetrahedral elements, with a maximum mesh size of $\lambda/6$ (LU, 2014), where $\lambda = \frac{2\pi f}{c}$, with f representing the frequency and c representing the velocity.

In Fig. 5b, a comparison of the TS for the verification model, covered with anechoic coatings with cylindrical cavities, is presented between the FEM results and KA solutions, when α is 0° . In the frequency range of 200 Hz–3 kHz, the average values of the results calculated by the FEM and the KA method are -13.75 and -13.61 dB, respectively. This validates the accuracy of the KA method in modeling the acoustic scattering of underwater vehicles with anechoic coatings containing cavities. The total calculation time of the FEM is 25.391 s, while the KA method only takes 15.35 s, indicating that the computational speed of the KA method is roughly 1654 times faster than the FEM method. This significant difference highlights the rapidity of the KA method. The research process of this study is shown in Fig. 6.

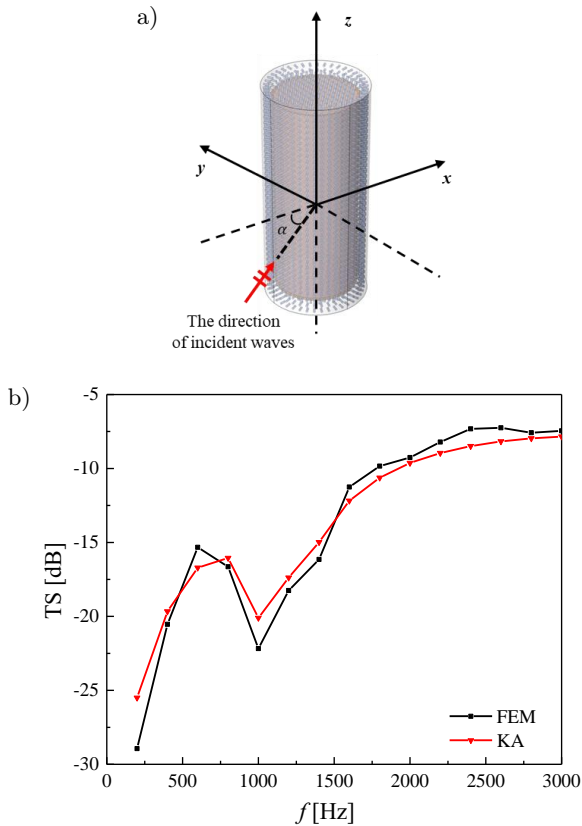


Fig. 5. a) Verification model; b) comparison of the FEM results and the KA solutions.

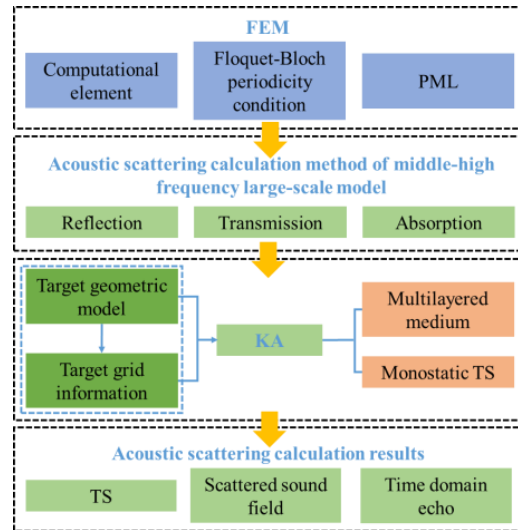


Fig. 6. Flow chart of acoustic scattering characteristics of underwater vehicle with Alberich coatings.

3. Numerical simulation of underwater vehicle with anechoic tiles

3.1. Reflection coefficients of different rubber structures

The reflection coefficients of homogeneous medium and rubber with air cavities at different angles and frequencies (f) are calculated by FEM, as shown in Fig. 7.

As illustrated in Fig. 7, the calculated frequency is in the range of 200 Hz–20 kHz with a step of 200 Hz. The cavity significantly impacts the acoustic characteristics of the anechoic tile. The resonance effect of

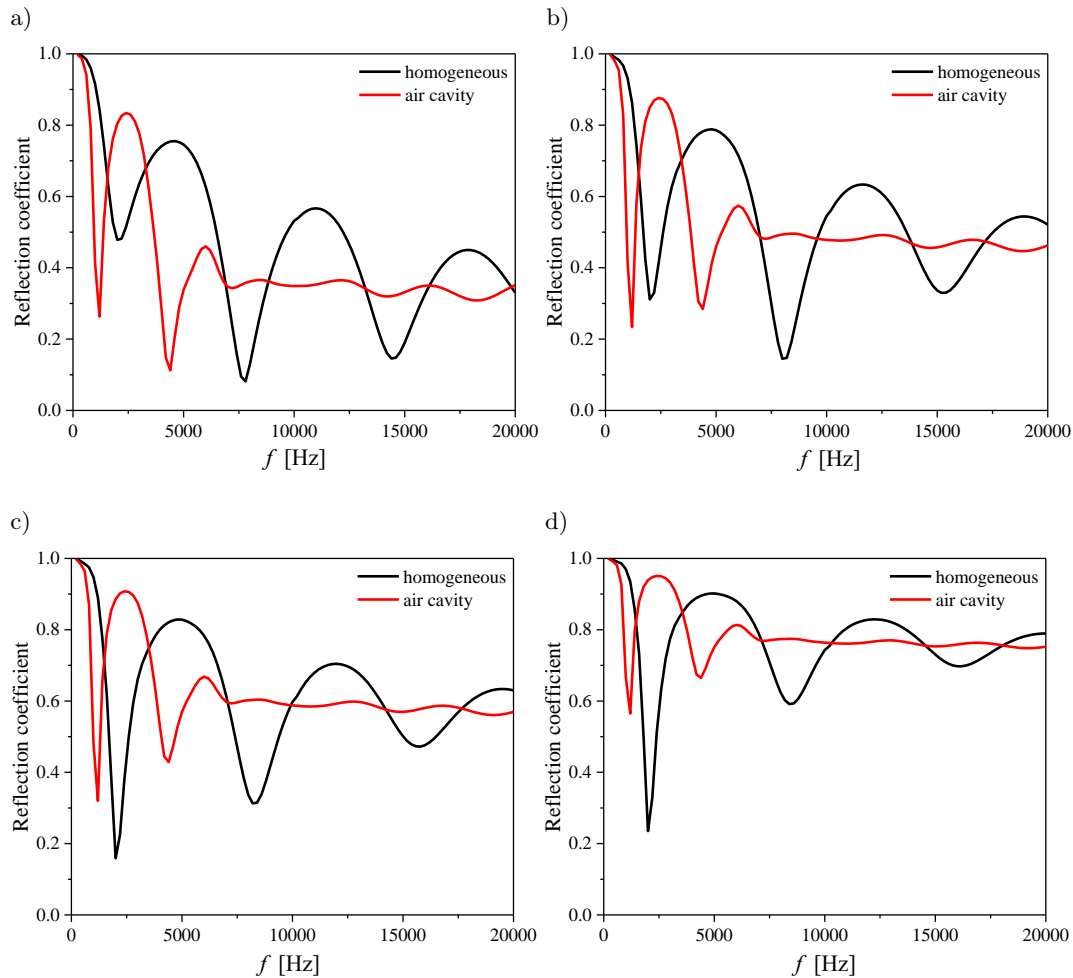


Fig. 7. Comparison of reflection coefficients of different anechoic tiles at different angles: a) 0° ; b) 45° ; c) 60° ; d) 75° .

the cavity not only accelerates the convergence speed of the reflection coefficient but also makes the reflection peak to move towards the low-frequency direction, which enhances the middle and low-frequency performance of the structure. The cavity structure makes the reflection coefficient more stable in the high frequency range. However, in practical applications, anechoic tiles with air cavities generally require more complex processing and manufacturing procedures compared to homogeneous medium anechoic tiles. Additionally, as the depth of the submarine increases, the pressure of the seawater medium also rises, leading to alterations in the acoustic performance of anechoic tiles with air cavities.

3.2. TS of the submarine model with homogeneous rubber and rubber with periodic internal cavities

The reflection coefficients, as shown in Fig. 7, are substituted into the KA method to obtain the TS of the benchmark model after applying different kinds of anechoic tiles. This process yields a TS angle-frequency

spectrum, with the horizontal axis representing the angle, and the vertical axis representing the frequency.

As shown in Fig. 8, different types of anechoic tiles exhibit varying degrees of suppression on the TS of underwater vehicles at different incident angles and frequencies. Similar to the trends observed in the reflection coefficient, anechoic tiles with periodic internal cavities demonstrate superior sound absorption in the low and specific middle frequency ranges compared to homogeneous mediums under the resonant interaction of the air cavity.

In Fig. 9, the directivity diagrams of TS for the benchmark model are presented at different frequencies before and after the applications of anechoic tiles, and the figure also illustrates the impact of different types of anechoic tiles on the TS of the model.

In Fig. 9, the variation trend of the TS presents a butterfly shape with the azimuth angle changing. The highest TS values are observed in the abeam direction of the underwater vehicle, primarily due to mirror reflections on the hull surface and acoustic reflections from the conning tower. With the existence

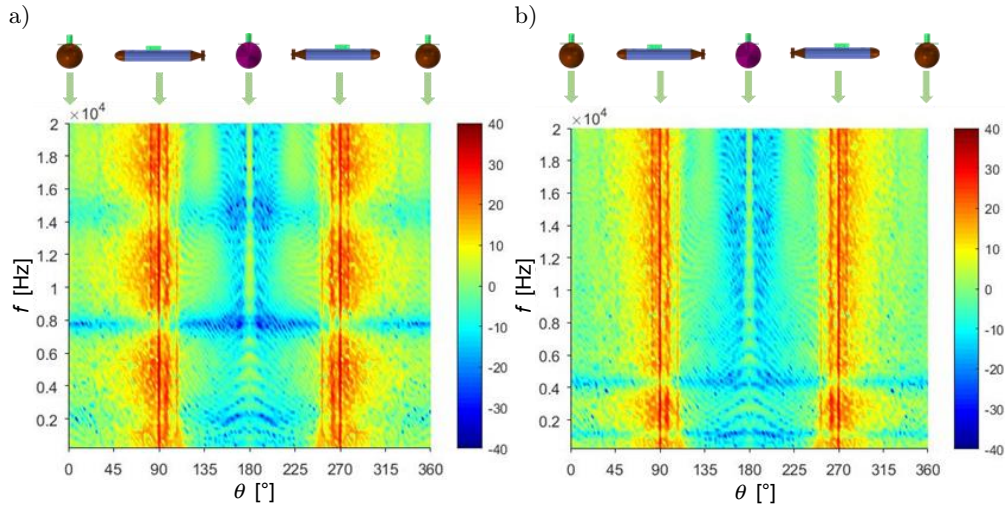


Fig. 8. TS angle-frequency spectrum of benchmark model with different anechoic tiles: a) homogeneous medium anechoic tiles; b) anechoic tiles with air cavities.

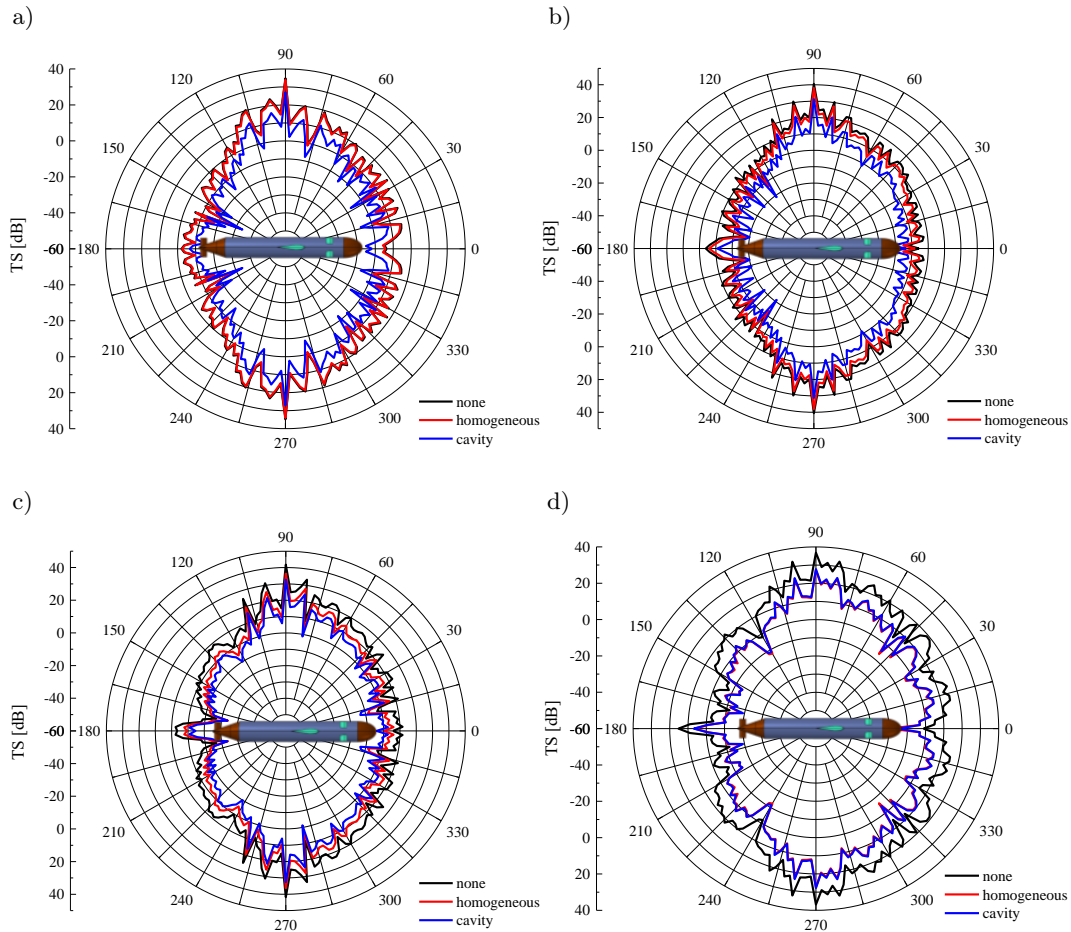


Fig. 9. TS directional diagrams of benchmark model with different anechoic tiles at different frequencies: a) 1 kHz; b) 5 kHz; c) 10 kHz; d) 20 kHz.

of cavity resonance, anechoic tiles with air cavities exhibit a more effective sound absorption effect compared to anechoic tiles with homogeneous mediums, partic-

ularly in the middle and low frequency ranges. Under the condition of high frequency, the silencing effect of different anechoic tiles becomes consistent.

4. Comparisons of acoustic scattering characteristics between the KA solutions and experimental results

4.1. Acoustic scattering characteristic test instrument and arrangement

By conducting a lake test of the benchmark scale model with anechoic tiles, the variation of echo characteristics concerning the horizontal azimuth and frequency of the incident wave is quantitatively analyzed, providing data support for verifying the accuracy of the KA method. Figure 10 shows the benchmark scale model and the test site.



Fig. 10. Benchmark scale model and test site photos.

According to Fig. 11, the Agilent 33220A signal generator is primarily employed to produce acoustic signals with specified parameters, including frequency, amplitude, and pulse width. The JYH1000A power amplifier amplifies the acoustic signals generated by the signal generator to ensure that the transmitted signals meet the requirements for underwater acoustic detection. The transducer converts the electrical signal into the acoustic signal and transmits it for target detection. The hydrophone is the device that converts the acoustic signal into an electrical signal, utilized for receiving the echo signal from the underwater model and converting it into an electrical representation. The charge amplifier amplifies the echo signal from the hydrophone. The China Orient Institute of Noise & Vibration INV3062A1 data acquisition system is responsible for receiving and storing the output echo signal from the charge amplifier, allowing for subsequent analysis and interpretation. The specific parameters of the benchmark model are shown in Fig. 3b. The scaling ratio used in this experiment, relative to the original model, is 1:15. The thickness of the shell is 3 mm, the length is 4.13 m, and the radius of the midship is 0.25 m. The signal pulse width is set to 1.5 ms, the signal length is 500 ms, and the sampling frequency is 80 kHz. Anechoic tiles with a homogeneous medium are laid on the surface of the experimental model. The thickness of each anechoic tile is 10 mm, and its Young's modulus, density and Poisson's ratio are 4.41×10^6 Pa, 1100 kg/m^3 and 0.48, respectively. The transmitting transducer, hydrophone, and research model are aligned in a straight line. The distance between the transducer and the hydrophone is 7.15 m, and the distance between the hydrophone and the research model is 3.65 m. All three are located at an underwater depth of 8.95 m. At the beginning of the test, it is ensured that the research model is facing the transducer in the abeam direction, and a horizontal uniform rotation of 360° during the rotation process is maintained.

4.2. Benchmark scale model monostatic TS experimental data analysis

The TS azimuth characteristics of the benchmark scale model obtained by the experiment and the KA method are shown in Fig. 12.

As illustrated in Fig. 12, the TS is highest in the abeam direction, which is $-7 \sim -3$ dB. In the bow direction it is $-14 \sim -6$ dB, and in the stern direction it is the smallest, measuring $-16 \sim -9$ dB. It can be seen that except for the range of $210 \sim 330^\circ$, the KA solutions are basically consistent with the experimental results in trend and magnitude, demonstrating the reliability of the KA method in predicting the monostatic TS of underwater vehicles with anechoic tiles. In the range of $210 \sim 330^\circ$, because of the model processing and suspension problems, there will be some discrepancies between the experimental results and the KA solutions.

4.3. Experimental data analysis of the time domain echo spreading characteristics of the benchmark scale model

The benchmark scale model with anechoic tiles used in the test has the directions of incident waves within the angle range of $0 \sim 360^\circ$ (where the abeam direction corresponds to incident directions of 0 and 180° , and the bow and stern correspond to 90 and 270° incident directions, respectively). The experimental results of time domain echo characteristics in different frequency ranges are compared to the KA solutions.

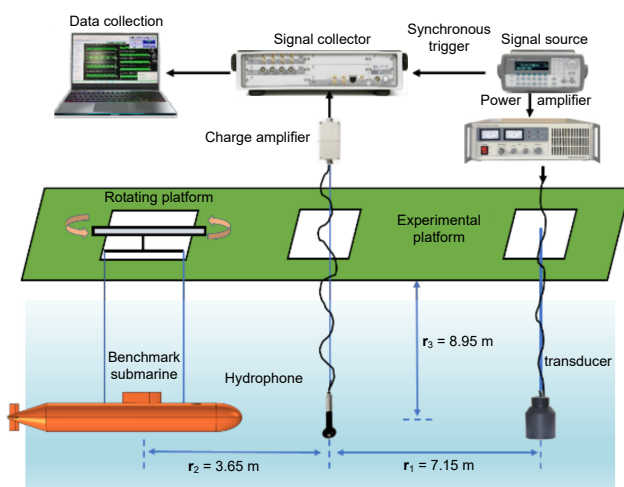


Fig. 11. Schematic diagram of the test equipment arrangement.

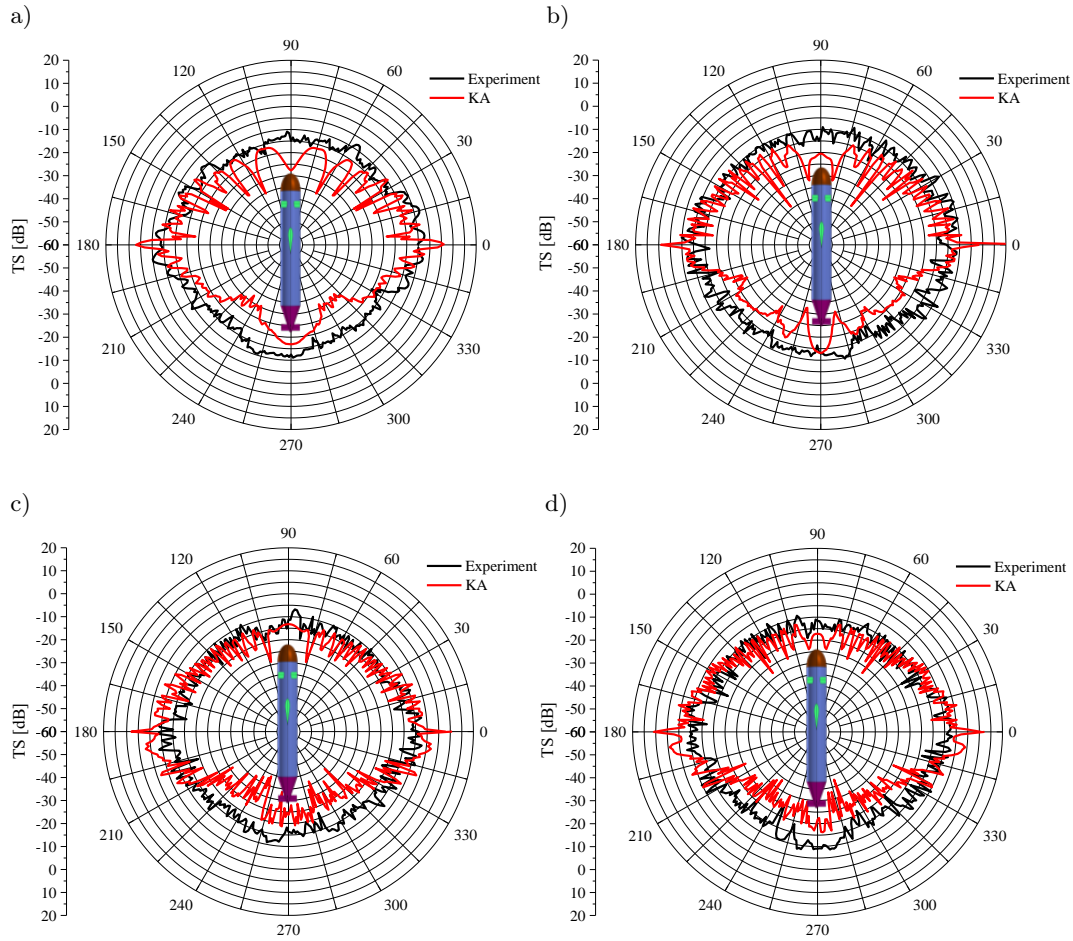


Fig. 12. Comparisons of TS between the experimental results and the KA solutions at different frequencies: a) 5 kHz; b) 10 kHz; c) 15 kHz; d) 20 kHz.

The comparisons of acoustic scattering echo characteristics between the benchmark submarine scale model' experimental results and KA solutions are shown in Figs. 13 and 14. Echo characteristics of the bow, elevator, conning tower and stern of the model

can be clearly observed in the experimental results and KA solutions, and the characteristics of each component can be accurately reflected in the echo time. However, there are still some differences between the experimental results and KA solutions. For example,

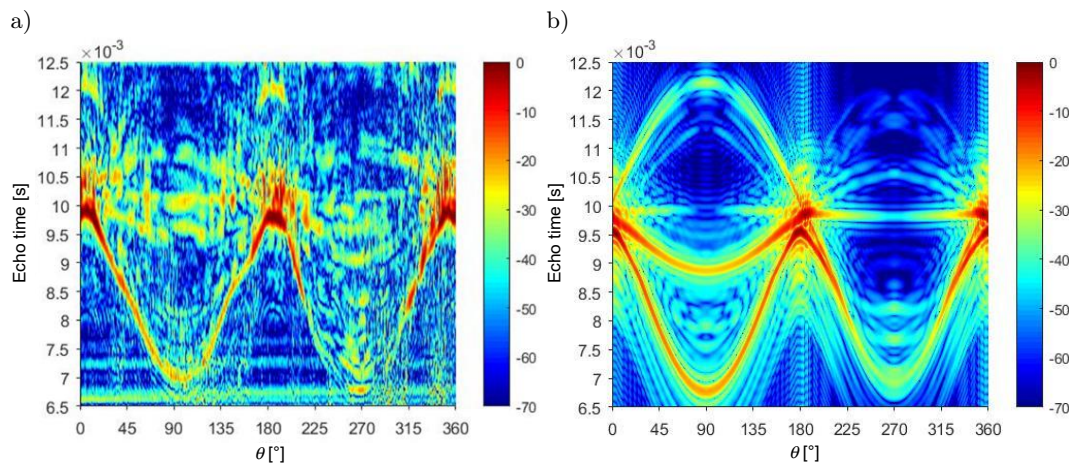


Fig. 13. Comparisons of the echo characteristics of the benchmark submarine scale model with anechoic tiles in the frequency band of 1–10 kHz between the experimental results and KA solutions: a) experimental results; b) KA solutions.

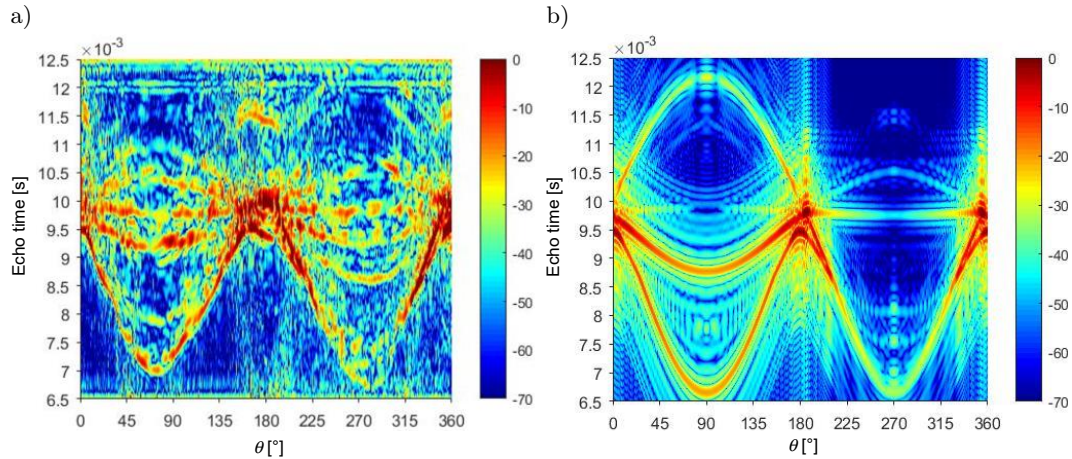


Fig. 14. Comparisons of the echo characteristics of the benchmark submarine scale model with anechoic tiles in the frequency band of 10–20 kHz between the experimental results and the KA solutions: a) experimental results; b) KA solutions.

the experimental results exhibits obvious highlights in the position of the elevator, and there are several more characteristic curves near the abeam direction which are presumed to be the echo characteristics from ropes, buckles and the beam used when hoisting the model. The above factors make the experimental results have more echo characteristics than the KA solutions.

5. Conclusions

In this study, the KA method is used to evaluate the TS and echo characteristics of a target after laying anechoic tiles. The rapidity and accuracy of the KA method are confirmed through comparisons with FEM and experimental results. This investigation achieves fast acoustic scattering prediction for targets with anechoic tiles, which makes a significant contribution to improving the acoustic stealth technology of the underwater vehicle.

From the research on underwater vehicles with anechoic tiles, we can come to the following conclusions.

The cavity significantly affects the resonance characteristics of anechoic tiles, especially in the case of vertical incidence, which not only reduces the reflection coefficient peaks, but also makes the reflection coefficient peaks move to the low frequency direction. This trend becomes more pronounced at frequencies below 10 kHz. However, acoustic tiles with internal cavities also require more complex processing and manufacturing processes, and the acoustic performance exhibits greater sensitivity to changes in environmental conditions, such as sound pressure. Therefore, in practical applications, a thorough assessment of the advantages and disadvantages of both methods is imperative to ensure the selection of an acoustic tile design that aligns with specific requirements.

In the experimental results and KA solutions, the TS and echo characteristics of the benchmark submarine model with anechoic tiles at different incident frequencies are approximately consistent. The benchmark submarine model with anechoic tiles can produce clear echo characteristics at the bow, elevator, conning tower, hull, and empennage, and several echo curves of the experimental results and KA solutions exhibit good agreement in terms of echo time, brightness, and shape. This alignment accurately reflects the external characteristics of the submarine model with anechoic tiles.

By investigating the sound absorption characteristics of anechoic tiles with cavities, we have gained profound insights into detection and stealth capabilities of underwater vehicles. The KA method enables rapid and precise evaluation of the TS after the application of anechoic tiles with periodic internal cavities. The significant reduction in computational time provides an efficient tool for the acoustic parameter design and optimization of anechoic tiles, thereby advancing underwater vehicle acoustic stealth and detection technology.

Acknowledgments

We acknowledge the support of the National Natural Science Foundation of China (52201397) and the Stability Support Project of the Laboratory of Science and Technology on Integrated Logistics Support (WDZC20235250311).

References

1. ABAWI A.T. (2016), Kirchhoff scattering from non-penetrable targets modeled as an assembly of triangular facets, *The Acoustical Society of America*, **140**(3): 1878–1886, doi: [10.1121/1.4962735](https://doi.org/10.1121/1.4962735).

2. CHEN X., LUO Y. (2018), Simulation of scattering acoustic field of underwater target in low frequency based on ANSYS and SYSNOISE [in Chinese], *Journal of Ordnance Equipment Engineering*, **39**(5): 103–107, doi: [10.11809/bqzbgcxb2018.05.022](https://doi.org/10.11809/bqzbgcxb2018.05.022).
3. ESFAHANI I.C., JI S., SUN H. (2023), A drop-on-micropillars (DOM) based acoustic wave viscometer for high viscosity liquid measurement, *IEEE Sensors Journal*, doi: [10.1109/JSEN.2023.3309757](https://doi.org/10.1109/JSEN.2023.3309757).
4. ESFAHANI I.C., SUN H. (2023), A droplet-based micropillar-enhanced acoustic wave (μ PAW) device for viscosity measurement, *Sensors and Actuators A: Physical*, **350**: 114121, doi: [10.1016/j.sna.2022.114121](https://doi.org/10.1016/j.sna.2022.114121).
5. FAN J., TANG W.L. (1999), The planar element method for computing target strength (TS) of sonar [in Chinese], *Proceedings of the Acoustical Society of China 1999 Youth Conference*, pp. 40–41.
6. FAN J., TANG W.L., ZHUO L.K. (2012), Planar elements methods for forecasting the echo characteristics from sonar targets, *Ship Mechanics*, **16**(1–2): 171–180, doi: [10.3969/j.issn.1007-7294.2012.01.020](https://doi.org/10.3969/j.issn.1007-7294.2012.01.020).
7. FAN J., ZHUO L.K. (2006), Graphical acoustics computing method for echo characteristics calculation of underwater targets, *Acta Acustica*, **31**(6): 511–516, doi: [10.3321/j.issn:0371-0025.2006.06.006](https://doi.org/10.3321/j.issn:0371-0025.2006.06.006).
8. FENG X.L., CHEN N.R., LI X.W., LI J. (2018), Analyzing the target strength of Benchmark submarine by boundary element method at low and middle frequencies [in Chinese], *Technical Acoustic*, **37**(05): 418–424, doi: [10.16300/j.cnki.1000-3630.2018.05.003](https://doi.org/10.16300/j.cnki.1000-3630.2018.05.003).
9. HUANG L.Z., XIAO Y., WEN J.H., YANG H.B., WEN X.S. (2015), Analysis of decoupling mechanism of an acoustic coating layer with horizontal cylindrical cavities [in Chinese], *Acta Physica Sinica*, **64**(15): 154301, doi: [10.7498/aps.64.154301](https://doi.org/10.7498/aps.64.154301).
10. LAVIA E., GONZALEZ J.D., BLANC S. (2018), Modelling high-frequency backscattering from a mesh of curved surfaces using Kirchhoff Approximation, *Journal of Theoretical and Computational Acoustics*, **27**(04): 17, doi: [10.1142/S2591728518500573](https://doi.org/10.1142/S2591728518500573).
11. LEE K., SEONG W. (2009), Time-domain Kirchhoff model for acoustic scattering from an impedance polygon facet, *The Acoustical Society of America*, **126**(1): 14–21, doi: [10.1121/1.3141887](https://doi.org/10.1121/1.3141887).
12. LIU B. (2020), *Research on acoustic scattering characteristics of typical structures of MUUV* [in Chinese], Shanghai Jiao Tong University, doi: [10.27307/d.cnki.gsjtu.2020.002589](https://doi.org/10.27307/d.cnki.gsjtu.2020.002589).
13. LIU H., PENG Z.L., FAN J., WU K. (2019), Numerical and experimental research on acoustic scattering time-frequency characteristics of dock landing ship [in Chinese], *Technical Acoustics*, **38**(02): 147–152, doi: [10.16300/j.cnki.1000-3630.2019.02.006](https://doi.org/10.16300/j.cnki.1000-3630.2019.02.006).
14. LIU J.W., PENG Z.L., FAN J., LIU Y., KONG H.M. (2023), Acoustic scattering prediction method of underwater vehicles based on slice-parameterized multi-highlight model, *Acta Armamentarii*, **44**(02): 517–525, doi: [10.12382/bgxb.2021.0764](https://doi.org/10.12382/bgxb.2021.0764).
15. LU D. (2014), *Researches on acoustic scattering of elastic target on finite element methods* [in Chinese], Harbin Engineering University.
16. MARSTON P.L., SUN N.H. (1995), Backscattering near the coincidence frequency of a thin cylindrical shell: Surface wave properties from elasticity theory and an approximate ray synthesis, *The Acoustical Society of America*, **92**(6): 777–783, doi: [10.1121/1.412124](https://doi.org/10.1121/1.412124).
17. NELL C.W., GILROY L.E. (2003), *An improved BASIS model for the BeTSSi submarine*, DRDC Atlantic TR, Technical report.
18. PIGNIER J.N., O'REILLY J.C., BOIJ S. (2015), A Kirchhoff approximation-based numerical method to compute multiple acoustic scattering of a moving source, *Applied Acoustics*, **96**: 108–117, doi: [10.1016/j.apacoust.2015.03.016](https://doi.org/10.1016/j.apacoust.2015.03.016).
19. TONG Y.Z., FAN J., WANG B. (2020), Application of Floquet-Bloch theory in dispersion curve calculation [in Chinese], *Technical Acoustics*, **39**(01): 11–14, doi: [10.16300/j.cnki.1000-3630.2020.01.002](https://doi.org/10.16300/j.cnki.1000-3630.2020.01.002).
20. WANG W.H., WANG B., FAN J., ZHOU J. (2021), An iterative planar elements method for calculating multiple acoustic scattering from concave targets, *Proceedings of the 18th Symposium on Underwater Noise of Ships*, pp. 121–126, doi: [10.26914/c.cnkihy.2021.056714](https://doi.org/10.26914/c.cnkihy.2021.056714).
21. WEI K.N., LI W., LEI M., CHAI Y.B. (2013), Simulation research on acoustic scattering characteristics of underwater targets based on boundary element method [in Chinese], *Proceedings of the Fourteenth Symposium on Underwater Noise of Ships*, pp. 452–462.
22. WITOS F. (2019), Properties of amplitude distributions of acoustic emission signals generated in pressure vessel during testing, *Archives of Acoustics*, **44**(3): 493–503, doi: [10.24425/aoa.2019.129264](https://doi.org/10.24425/aoa.2019.129264).
23. XU H.T., AN J.Y., LIU C.F. (2004), Acoustic characteristics of anechoic coatings containing air cavities in water [in Chinese], *Technical Acoustics*, **23**(z1): 345–347, doi: [10.3969/j.issn.1000-3630.2004.z1.101](https://doi.org/10.3969/j.issn.1000-3630.2004.z1.101).
24. XU Z.C., ZHANG M.M., WANG L. (2015), Numerical simulation of acoustic scattering at low frequency for the BeTSSi submarine [in Chinese], *Computer & Digital Engineering*, **43**(04): 551–553+575, doi: [10.3969/j.issn1672-9722.2015.04.003](https://doi.org/10.3969/j.issn1672-9722.2015.04.003).
25. YAO X.L., ZHANG Y., QIAN D.J., HUANG C., ZHANG H.H. (2007), Characteristics analysis of acoustic insulation and decoupled tiles by FEM and experiment [in Chinese], *Chinese Journal of Ship Research*, **2**(6): 9–15, doi: [10.3969/j.issn.1673-3185.2007.06.003](https://doi.org/10.3969/j.issn.1673-3185.2007.06.003).
26. ZHENG G.Y., FAN J., TANG W.L. (2011), A modified planar elements method considering occlusion and secondary scattering [in Chinese], *Acta Acustica*, **36**(4): 377–383, doi: [10.15949/j.cnki.0371-0025.2011.04.010](https://doi.org/10.15949/j.cnki.0371-0025.2011.04.010).